Cations Distribution and Valence States in Mn-Substituted $Li_4Ti_5O_{12}$ Structure

Doretta Capsoni,[†] Marcella Bini,[†] Vincenzo Massarotti,*[,†] Piercarlo Mustarelli,[†] Gaetano Chiodelli,[‡] Carlo B. Azzoni,[§,⊥] Maria C. Mozzati,[§] Laura Linati,[||] and Stefania Ferrari[†]

Department of Physical Chemistry "M. Rolla", University of Pavia, viale Taramelli 16, 27100 Pavia, Italy, CNR-IENI Sezione di Pavia, viale Taramelli 16, 27100 Pavia, Italy, CNISM, Department of Physics "A. Volta", University of Pavia, via Bassi 6, 27100 Pavia, Italy, and Centro Grandi Strumenti, University of Pavia, via Bassi 21, 27100 Pavia, Italy

Received December 21, 2007. Revised Manuscript Received April 11, 2008

Structure, cation distribution, Mn oxidation states, and conductivity behavior of the Mn-substituted (up to 30% of Ti ions) $Li_4Ti_5O_{12}$ have been investigated by the combined use of X-ray powder diffraction, electron paramagnetic resonance (EPR), ^{7}Li MAS NMR, and impedance spectroscopy techniques. The spinel structure of the lithium titanate is preserved and the lattice parameter decreases with increasing the Mn content. Mn^{2+} ions progressively occupy the tetrahedral site up to an approximately constant value reached for 10% Mn-substituted samples. Mn^{3+} ions occupy both octahedral and tetrahedral sites, with a constant value on the tetrahedral one, independent of the total Mn amount; Mn^{4+} ions are not detected. The Mn^{2+} paramagnetic ions give rise to a through-space interaction with Li^+ ions of both cationic sites, as evaluated by the area, proportional to the Mn^{2+} ions content, of a peak at ∼8 ppm observed in the ^{7}Li NMR spectra for the substituted samples. The obtained cation distribution and the Mn valence states satisfactorily explain the decrease of conductivity observed in the Mn-doped samples with respect to the pure $Li_4Ti_5O_{12}$.

1. Introduction

$Li_4Ti_5O_{12}$, also reported as $Li_{1.333}Ti_{1.667}O_4$, is a promising anode material for rechargeable lithium ion batteries.[1,2] The tetrahedral Li^+ ions, located on the 8a sites of the cubic spinel structure (*Fd*3*m* S.G.), can move to the octahedral 16c empty sites, leading to an easy reversible intercalation−deintercalation mechanism, assured by the stable $Li_4Ti_5O_{12}$ framework, with lattice parameters practically unchanged during cell cycling.[3,4] The recent research focuses on the optimization of the electrochemical features starting from polycrystalline,[5] nanocrystalline,[6–10] or thin films[11] $Li_4Ti_5O_{12}$ samples. Moreover, both theoretical[12] and experimental[13–26] studies were carried out on doped compounds, in a wide compositional range, to improve the low electronic conductivity[26] of the material.

The iron substitution was widely investigated:[13–16] the Fe distribution on tetrahedral and octahedral sites and the phase transition to the ordered spinel structure ($P4_332$ S.G.), as a

* To whom correspondence should be addressed. Phone: +39-382-987203. Fax: +39-382-987575. E-mail: vincenzo.massarotti@unipv.it.
[†] Department of Physical Chemistry "M. Rolla", University of Pavia.
[‡] CNR-IENI Sezione di Pavia.
[§] CNISM, Department of Physics "A. Volta", University of Pavia.
[||] Centro Grandi Strumenti, University of Pavia.
[⊥] Passed away on the 30th of August 2007.

(1) Goodenough, J. B.; Manthiram, A.; Wnetrzewski, B. *J. Power Sources* **1993**, *43–44*, 269.
(2) Koksbang, R.; Barker, J.; Shi, H.; Saidi, M. Y. *Solid State Ionics* **1996**, *84*, 1.
(3) Scharner, S.; Weppner, W.; Schmid-Beurmann, P. *J. Electrochem. Soc.* **1999**, *146*, 857.
(4) Jansen, A. N.; Kahaian, A. J.; Kepler, K. D.; Nelson, P. A.; Amine, K.; Dees, D. W.; Vissers, D. R.; Thackeray, M. M. *J. Power Sources* **1999**, *81–82*, 902.
(5) Wang, G. X.; Bradhurst, D. H.; Dou, S. X.; Liu, H. K. *J. Power Sources* **1999**, *83*, 156.
(6) Bach, S.; Pereira-Ramos, J. P.; Baffier, N. *J. Mater. Chem.* **1998**, *8*, 251.
(7) Hao, Y.; Lai, Q.; Liu, D.; Xu, Z.; Ji, X. *Mater. Chem. Phys.* **2005**, *94*, 382.
(8) Hao, Y.; Lai, Q.; Xu, Z.; Liu, D.; Ji, X. *Solid State Ionics* **2005**, *176*, 1201.
(9) Venkateswarlu, M.; Chen, C. H.; Do, J. S.; Lin, C. W.; Chou, T. C.; Hwang, B. J. *J. Power Sources* **1995**, *146*, 204.
(10) Hao, Y.; Lai, Q.; Lu, J.; Wang, H.; Chen, Y.; Ji, X. *J. Power Sources* **2006**, *158*, 1358.
(11) Rho, J. H.; Kanamura, K.; Umegaki, T. *Chem. Lett.* **2001**, *30*, 1322.
(12) Liu, D.; Ouyang, C.; Shu, J.; Jiang, J.; Wang, Z.; Chen, L. *Phys. Status Solidi B* **2006**, *243*, 1835.
(13) Robertson, A. D.; Trevino, L.; Turamoto, H.; Irvine, J. T. S. *J. Power Sources* **1999**, *81–82*, 352.
(14) Robertson, A. D.; Turamoto, H.; Irvine, J. T. S. *J. Electrochem. Soc.* **1999**, *146*, 3958.
(15) Scharner, S.; Weppner, W.; Schmid-Beurmann, P. *J. Solid State Chem.* **1997**, *134*, 170.
(16) Reale, P.; Panero, S.; Ronci, F.; Rossi Albertini, V.; Scrosati, B. *Chem. Mater.* **2003**, *15*, 3437.
(17) Jovic, N.; Antic, B.; Kremenovic, A.; Spasojevic-de Bire, A.; Spasojevic, V. *Phys. Status Solidi A* **2003**, *198*, 18.
(18) Nakayama, M.; Ishida, Y.; Ikuta, H.; Wakihara, M. *Solid State Ionics* **1999**, *177*, 265.
(19) Ohzuku, T.; Tatsumi, K.; Matoba, N.; Sawai, K. *J. Electrochem. Soc.* **2000**, *147*, 3592.
(20) Huang, S.; Wen, Z.; Zhu, X.; Lin, Z. *J. Electrochem. Soc.* **2005**, *152*, A186.
(21) Hernandez, V. S.; Torres Martinez, L. M.; Mather, G. C.; West, A. R. *J. Mater. Chem.* **1996**, *6*, 1533.
(22) Leonidov, I. A.; Leonidova, O. N.; Samigullina, R. F.; Patrakeev, M. V. *J. Struct. Chem.* **2004**, *45*, 262.
(23) Kubiak, P.; Garcia, A.; Womes, M.; Aldon, L.; Olivier-Fourcade, J.; Lippens, P. E.; Jumas, J. C. *J. Power Sources* **2003**, *119–121*, 626.
(24) Lambert, P. M.; Harrison, M. R.; Edwards, P. P. *J. Solid State Chem.* **1988**, *75*, 332.

10.1021/cm703650c CCC: $40.75
Published on Web 06/11/2008

function of Fe amount, were studied and the electrochemical behavior was completely characterized. Interesting results were also obtained on Co-,[17] Ni-,[13] Cr-,[18,19] Al-,[20] Mg-,[26]and Zn-substituted[21,22] samples.

The Mn substitution on Ti ions was also studied:[23] the authors, on the basis of XAS measurements, claim that "Mn is located as Mn(IV) probably on both tetrahedral and octahedral sites". On the other hand, the Mn substitution on Li ions in $LiTi_2O_4$ showed the formation of Mn^{2+} ions with electroneutrality achieved by a proper Ti^{3+}/Ti^{4+} ratio.[24] The presence of Mn^{2+} ions is also evidenced by Ti^{4+} substitution in the $LiMn_2O_4$ spinel structure.[25] The +4 oxidation state is expected for the Mn ions in the $Li_4Mn_5O_{12}$ compound, isostructural with $Li_4Ti_5O_{12}$; however, difficulties are reported in the literature[27–29] for preparing the stoichiometric sample, due to its instability with temperatures higher than 893 K. In fact, even in a highly oxidizing atmosphere (10 atm O_2 flux), the partial reduction of Mn^{4+} to Mn^{3+} is observed, the Mn mean oxidation state is +3.8, and the formation of oxygen vacancies is taken into account to achieve the charge balance.

In the present work the influence of Mn substitution (up to 30%) on the $Li_{1.333}Ti_{1.667}O_4$ structure and on its electrical behavior is investigated, in order to give new insights into cation distribution, Mn valence state, and local arrangement, relating them to the transport properties. This purpose will be reached through the combined use of X-ray powder diffraction (XRPD) with structural refinement, electron paramagnetic resonance (EPR), and solid state ^{7}Li nuclear magnetic resonance (NMR) spectroscopy. The conductivity behavior of pure and doped samples will be investigated by means of impedance spectroscopy (IS) measurements.

2. Experimental Methods

The $Li_4Ti_5O_{12}$ sample was prepared via solid state synthesis from a stoichiometric Li_2CO_3 (Aldrich, 99.6%) and TiO_2 (Merck, >99%) mixture. A 3% Li_2CO_3 weight excess was used to prevent Li_2O sublimation during the thermal treatment, as suggested in the literature.[20] The mixture was treated for 60 h at 1073 K in air with two intermediate grindings.

The Mn-doped samples were prepared following the same procedure by adding MnO (Alfa, 99.5%) (A, B, and C samples) or MnO_2 (D and E samples, thermal treatment in air and O_2 flow, respectively) in the proper amount to reach a Mn substitution on the cationic framework of 3, 10, 15, and 30% of 1.667, i.e., the Ti amount present in the pure sample. Since the Mn ion is stable in different oxidation states and our thermal treatments are performed in air starting from the MnO precursor, the $Li_{1.333-x/3}Mn_xTi_{1.667-2x/3}O_4$, $Li_{1.333-x/6}Mn_xTi_{1.667-5x/6}O_4$ and $Li_{1.333}Mn_xTi_{1.667-x}O_4$ ($x = 0.05$, 0.167, 0.25, and 0.50 for 3, 10, 15, and 30% substituted samples) formulas are used in the hypothesis that only Mn^{3+} (A), Mn^{3+}/Mn^{4+} in equal amount (B), or only Mn^{4+} (C, D, and E) are formed, respectively. In the following, each sample will be indicated by the respective substituted percentage and the letter related to the previously reported meaning.

Room temperature (r.t.) XRPD measurements were performed in air on a Bruker D5005 diffractometer with the Cu Kα radiation, Ni filter, and a position-sensitive detector (PSD). Rietveld structural and profile refinement was carried out by means of the TOPAS V3.0 program.[30]

EPR measurements were performed at about 9.4 GHz at r.t. with a Bruker spectrometer. Particular care was paid in determining the sample mass and position in the resonant cavity to compare signal intensities (areas) with those of suitable standards (Varian Pitch and Li_2MnO_3) and to estimate the relative amount of the paramagnetic species in the samples. The derivative signal areas were computed by double integration with numerical methods.

The ^{7}Li NMR measurements were performed at r.t. and 155.6 MHz on a AMX400WB spectrometer (Bruker) based on a 9.4 T magnet. MAS spectra were acquired with a 4 mm probe head (Bruker), equipped with cylindrical zirconia rotors and a boron nitride stator. The samples were spun at 10.5 kHz and the data were averaged over 64 acquisitions using a single-pulse sequence, with a 90° pulse of 3 μs and a recycle time of 10 s. The spectra were referenced to an external sample of 1.0 M LiCl in H_2O.

The IS measurements were performed by means of a Frequency Response Analyzer (FRA) Solartron 1260 apparatus in the frequency range 10^{-3} to 10^7 Hz, with the experimental setting described elsewhere.[31] Conductivity measurements were carried out as a function of the temperature on disk-shaped samples sintered at 1073 K for 12 h, inserted in a polythermal electrochemical cell supplied by a guard circuit to minimize the noises. To ensure good electrical contact for the conductivity measurements, platinum electrodes were deposited by sputtering on the opposite flat surfaces of the pellets. The measurements were performed in gas flow (O_2, N_2) up to 1073 K, after the pellets pretreatment at 1073 K for 6 h in O_2, followed by cooling (5 K/min) down to r.t.

3. NMR Theoretical Aspects

The NMR information of Li cathode materials has been deeply investigated during recent years. An excellent review was recently published by Grey and Duprè,[32] and the following discussion will largely rest on that paper. In compounds containing paramagnetic centers the nuclear spins I will interact with the time-averaged electronic magnetic moments, $<\mu_e>$, via (i) through-space (dipolar) interactions and (ii) through-bonds (Fermi-contact) interactions. As a matter of fact, if the electron *g* tensor is anisotropic, we must also consider the pseudocontact shift term (see below).

3.1. Dipolar Coupling (DP). This interaction is due to the magnetic fields of the electronic spins that are experienced by the nuclear spins I. The related electron-nucleus Hamiltonian, H_{en}, is given by

$$H_{en} = \frac{\mu_0}{4\pi}\langle \mu_e \rangle \mathbf{D_{en}} \mu_I$$

where μ_I is the magnetic moment of the nucleus and $\mathbf{D_{en}}$ is a second-rank tensor whose elements are defined as

(25) Petrov, K.; Rojas, R. M.; Alonso, P. J.; Amarilla, J. M.; Lazarraga, M. G.; Rojo, J. M. *Solid State Sci.* **2005**, *7*, 277.
(26) Chen, C. H.; Vaughey, J. T.; Jansen, A. N.; Dees, D. W.; Kahaian, A. J.; Goacher, T.; Thackeray, M. M. *J. Electrochem. Soc.* **2001**, *148*, A102.
(27) Kim, J.; Manthiram, A. *J. Electrochem. Soc.* **1998**, *145*, L53.
(28) Takada, T.; Hayakawa, H.; Akiba, E. *J. Solid State Chem.* **1995**, *115*, 420.
(29) Takada, T.; Hayakawa, H.; Kumagai, T.; Akiba, E. *J. Solid State Chem.* **1996**, *121*, 79.
(30) Bruker AXS. *TOPAS V3.0: General profile and structural analysis software for powder diffraction data. User Manual.*; Bruker AXS: Karlsruhe, Germany, 2005.
(31) Chiodelli, G.; Lupotto, P. *J. Electrochem. Soc.* **1991**, *9*, 2703.
(32) Grey, C. P.; Duprè, N. *Chem. Rev.* **2004**, *104*, 4493.

$$D_{ij} = \frac{1}{r^3}(\delta_{ij} - 3e_i e_j)$$

where r is the distance between the nuclear and electronic spins, δ_{ij} is the Kronecker symbol, and $e_{i,j}$ are the components of a unit vector directed from the nuclear spin to the electron one. In general, this term is only partially removed by MAS rotation, giving origin to characteristic spinning sidebands manifolds, which contain information on the size of the interaction and the spins orientation. The total DP Hamiltonian is obtained by means of the superposition principle.

3.2. Fermi-Contact (FC). This term is due to the unpaired electron spin density that is transferred, directly or indirectly (e.g., via oxygen orbitals in our case), from the paramagnet to the s orbital of the NMR-active atom. In the limit of short electronic lifetimes in the NMR time scale, the FC term gives a chemical shift

$$\delta = -\frac{A}{\omega_0 h}\langle S_z \rangle$$

where ω_0 is the Larmor frequency, $\langle S_z \rangle$ is the time-averaged electron spin projection along the quantization direction, and A/h is the hyperfine constant given by

$$A/h = \frac{g\mu_0\mu_B\gamma_N\rho(r=0)}{3S}$$

where ρ is the electron spin density at the nucleus, μ_B and γ_N are the Bohr magneton and the gyromagnetic ratio of the NMR-active spin, respectively, and the other symbols have their usual meaning. It must be stressed that A/h can be both positive and negative, chiefly depending on the bond angles. Also the FC interaction is generally additive, and the overall shift may be obtained by summing the shift induced by each magnetic ion.

3.3. Pseudocontact Shift (PS). If the paramagnetic ions have an anisotropic magnetic susceptibility, the total hyperfine shift is given by $\Delta H_{tot} = \Delta H_{FC} + \Delta H_{PS}$, where ΔH_{FC} is the Fermi-contact contribution and ΔH_{PS} is a pseudocontact shift given by McConnel and Robertson:[33]

$$\Delta H_{PS} = -\frac{(3\cos^2\phi)(g_{||}^2 - g_{\perp}^2)\mu_B^2 H_0 S(S+1)}{9kTR}$$

Here ϕ is the angle between the nucleus-paramagnet radius vector (of length R) and the principal magnetic axis, $g_{||}$ and $g_{\perp}$ are the components of the g tensor parallel and perpendicular to the radius vector, respectively, μ_B is the Bohr magneton, and the other symbols have their usual meaning.

4. Results

4.1. XRPD. The XRPD pattern of the pure sample is shown in Figure 1. All the peaks can be explained on the basis of the $Li_4Ti_5O_{12}$ expected reflections. In the doped samples, except for 3A and 10A, some additional weak peaks are observed: they can be attributed to traces of TiO_2 (rutile phase) and/or Li_2TiO_3 impurities. By increasing the dopant quantity, a higher amount of Li_2TiO_3 is observed together with the $LiMn_2O_4$ spinel phase, present only in the 15C and 30C samples. As an example, the patterns of the C samples

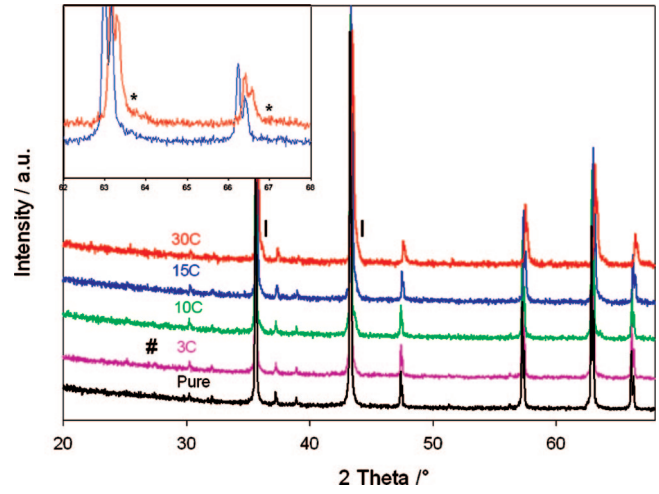

Figure 1. XRPD patterns of pure and doped samples (C series): the relevant peaks of Li_2TiO_3 (l), TiO_2 (#), and $LiMn_2O_4$ (*; see inset) impurity phases are indicated.

are shown in Figure 1. In the inset some peaks of the $LiMn_2O_4$ impurity phase are evidenced.

All the XRPD patterns were refined with the Rietveld method, starting from the spinel structure, where Ti occupies the octahedral site and Li both the octahedral and tetrahedral ones. For the doped samples the Mn ions occupy the octahedral site. Reliable results were obtained, even though with small negative values of the B thermal factors on the tetrahedral site. This suggested that the occupancy factors be refined under a suitable constraint: the Ti amount is fixed on the octahedral site, while Mn can also occupy the tetrahedral one and a corresponding amount of Li ions should be located on the octahedra. The main refined structural parameters, R_B and R_{wp} discrepancy factors, and goodness of fit[30] are reported in Table 1. The lattice parameter decreases with increasing the Mn content. Positive and reliable thermal factors are always obtained and satisfactory discrepancy factors are reached. In Table 2 the refined cations distribution and the impurity phase abundance are reported. The Mn amount on the tetrahedral site increases passing from 3 to 10% of dopant, and then it remains approximately constant. The TiO_2 phase is only present in traces in 3B and 3C samples, while Li_2TiO_3 increases its percentage with increasing the Mn amount. $LiMn_2O_4$ is only detected in 15C and 30C samples.

4.2. EPR. For the 3, 10, and 15% Mn-doped samples the EPR spectra (Figure 2) are very similar to those of Mn^{2+} ($3d^5$) ions in glass matrixes:[34] these signals show two main components with $g_{eff} \sim 4.3$ and with $g_{eff} \sim 2$, whose origin can be attributed to Mn^{2+} ions in different symmetry sites, i.e., with different E and D crystal field parameters values, greater or lower than $h\nu$, in the standard spin Hamiltonian. In all the 3% Mn-doped samples, six hyperfine lines are also evident, overlapped to the broad component with $g_{eff} \sim 2$, as shown in the inset of Figure 2a for the 3B sample, chosen as an example.

Signals coming from Mn^{3+} ($3d^4$) are not expected in our experimental configuration. As a matter of fact, indepen-

(33) McConnell, H. M.; Robertson, R. E. *J. Chem. Phys.* **1958**, *29*, 1361.

(34) Griscom, J. L. *J. Non-Cryst. Solids* **1980**, *40*, 211, and references therein.

Table 1. Lattice Parameters, Isotropic Thermal Factors of Tetrahedral, Octahedral, and Oxygen Sites, Oxygen Fractional Coordinate, Bragg and Weighted Pattern Discrepancy Factors, and Goodness of Fit Obtained by the Rietveld Refinement

sample	a /Å	B(tetr)/Å^2	B(oct)/Å^2	B(O)/Å^2	x(O)	R_B	R_{wp}	GoF
pure	8.3573(1)	2.4(4)	1.58(6)	1.61(7)	0.3873(1)	2.05	7.83	1.34
3A	8.3534(1)	2.9(4)	1.61(4)	1.61(7)	0.3872(2)	1.84	7.66	1.39
3B	8.3553(1)	2.9(4)	1.53(3)	1.64(6)	0.3872(1)	1.72	7.01	1.33
3C	8.3540(1)	2.9(4)	1.57(3)	1.62(6)	0.3876(1)	1.96	7.21	1.26
10A	8.3559(6)	3.1(4)	1.55(4)	1.53(7)	0.3871(2)	1.19	6.54	1.20
10B	8.3526(1)	2.4(4)	1.58(7)	1.71(7)	0.3878(2)	1.55	6.63	1.20
10C	8.3523(1)	2.6(4)	1.69(4)	2.07(7)	0.3871(2)	1.58	5.81	1.20
10D	8.3520(1)	2.4(3)	1.76(4)	2.04(6)	0.3873(1)	1.79	5.93	1.22
10E	8.3462(1)	3.2(4)	1.62(4)	2.07(7)	0.3872(2)	1.78	6.10	1.22
15C	8.3418(1)	3.0(4)	1.64(4)	2.21(7)	0.3879(2)	1.76	5.33	1.18
30C	8.3220(1)	2.7(5)	1.52(7)	2.21(10)	0.3879(2)	1.35	4.66	1.20

Table 2. Cation Distribution and Impurity Phases Weight Percentages Obtained by the Rietveld Refinement

sample	refined stoichiometry	TiO_2 %	Li_2TiO_3 %	$LiMn_2O_4$ %
pure	$[Li_1]_T[Li_{0.333}Ti_{1.667}]_OO_4$			
3A	$[Li_{0.981(4)}Mn_{0.019(4)}]_T[Li_{0.336(4)}Mn_{0.031(4)}Ti_{1.633}]_OO_4$			
3B	$[Li_{0.980(4)}Mn_{0.020(4)}]_T[Li_{0.336(4)}Mn_{0.030(4)}Ti_{1.625}]_OO_4$	0.7(2)	1.9(2)	
3C	$[Li_{0.985(4)}Mn_{0.015(4)}]_T[Li_{0.348(4)}Mn_{0.035(4)}Ti_{1.616}]_OO_4$	0.3(7)	2.0(1)	
10A	$[Li_{0.946(4)}Mn_{0.054(4)}]_T[Li_{0.332(4)}Mn_{0.112(4)}Ti_{1.556}]_OO_4$			
10B	$[Li_{0.963(4)}Mn_{0.037(4)}]_T[Li_{0.343(4)}Mn_{0.129(4)}Ti_{1.528}]_OO_4$		2.3(2)	
10C	$[Li_{0.965(4)}Mn_{0.035(4)}]_T[Li_{0.365(4)}Mn_{0.131(4)}Ti_{1.500}]_OO_4$		5.9(2)	
10D	$[Li_{0.965(4)}Mn_{0.034(4)}]_T[Li_{0.365(4)}Mn_{0.132(4)}Ti_{1.500}]_OO_4$		7.6(3)	
10E	$[Li_{0.972(4)}Mn_{0.027(4)}]_T[Li_{0.357(4)}Mn_{0.139(4)}Ti_{1.500}]_OO_4$		5.9(3)	
15C	$[Li_{0.965(4)}Mn_{0.035(4)}]_T[Li_{0.368(4)}Mn_{0.215(4)}Ti_{1.417}]_OO_4$		8.5(3)	0.3(1)
30C	$[Li_{0.964(5)}Mn_{0.037(5)}]_T[Li_{0.366(4)}Mn_{0.463(5)}Ti_{1.166}]_OO_4$		10.9(6)	6.3(4)

dently of the crystal field symmetry and possible site distortions due to Jahn−Teller effect, we have verified that the spin−orbit coupling breaks the ground-state spin degeneracy of the Mn^{3+} ion: this energy splitting is very small, compared with crystal field and distortion energies, but large enough to prevent spin resonance in the X-band microwave range. This result was obtained for Mn^{3+} in octahedral coordination in a previous work.[35] We have found an analogous result for Mn^{3+} in the tetrahedral site, calculating eigenvalues and eigenstates by diagonalizing the 25·25 matrix obtained from the Hamiltonian

$$H = H_{CF} + H_{SO} = -|e|V(\mathbf{r}) + \lambda \mathbf{L}\cdot\mathbf{S}$$

operating on the $|\mathbf{L}, \mathbf{M_L}, \mathbf{S}, \mathbf{M_S}>$ states of the ion (ground state ^{5}D), in which we assumed for the spin−orbit constant, λ, the value[36] of 88 cm^{-1} and inserted the coordinates (deduced from Table 1) of the oxygen ions forming the coordination tetrahedron whose center is the Mn^{3+} ion. From our calculations, the spin−orbit interaction produces a spin singlet ground state with an energy of about 5×10^{-3} eV with respect to the first excited level, indeed much higher than the microwave energy $h\nu$ of our EPR spectrometer ($h\nu \cong 3.8 \times 10^{-5}$ eV).

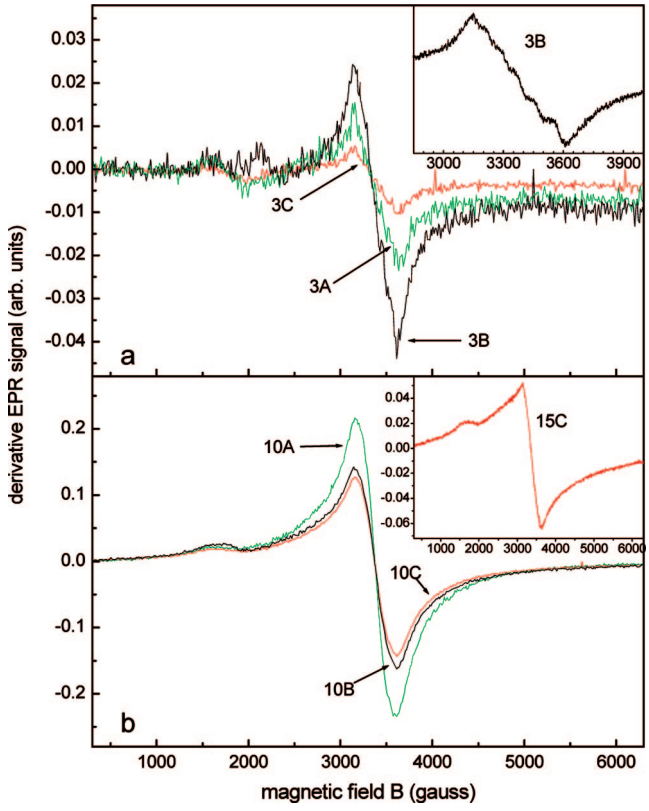

Figure 2. Representative r.t. EPR spectra of 3% (a), 10% (b), and 15% (inset of b) doped samples. The inset in (a) shows an enlarged view of the 3B sample spectrum, evidencing the presence of six lines of hyperfine structure.

No EPR signals from Mn^{4+} ($3d^3$) ion, expected both in tetrahedral and in octahedral coordination with $g < 2$,[36] are evident, suggesting that Mn ions with this oxidation state are not present in our samples. Indeed, the hyperfine structure observed for the 3% Mn-doped samples is centered on the broad line at $g_{eff} \sim 2$, observed for all the samples, suggesting that hyperfine structure and broad line have the same origin (the same g-factor). The main features of the hyperfine structure (quite broad line width of the "single" line and hyperfine splitting between the six lines of about 80−100G) allow us to ascribe this hyperfine structure, and so the whole observed signal, to Mn^{2+} ions.

For the 30C sample the EPR signal coming from the $LiMn_2O_4$ impurity (Table 2) does not allow reliable evaluation of signals coming from Mn ions in the doped $Li_{1.333}Ti_{1.667}O_4$ phase.

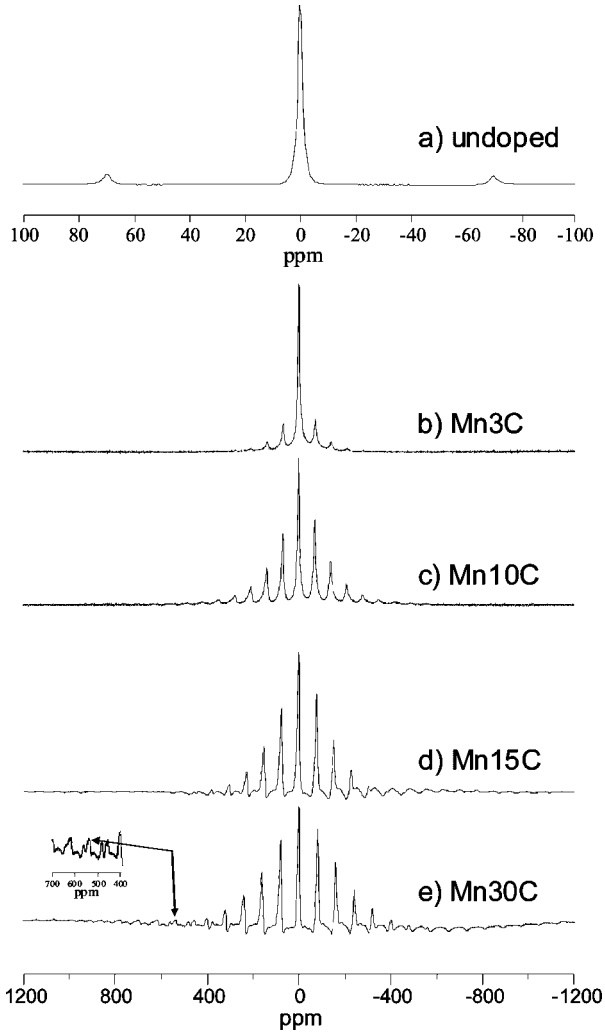

Figure 3. ^{7}Li MAS NMR spectra of some selected samples. The inset in part (e) shows the small peak of the $LiMn_2O_4$ spinel phase.

4.3. NMR. Figure 3 shows the spectra of some selected samples. The spectrum (a) of pure $Li_4Ti_5O_{12}$ is characterized by a relatively narrow (∼300 Hz) line due to diamagnetic lithium. In the limit of our experimental resolution, we are not able to separate the contributions of nuclei in tetrahedral (8a) and octahedral (16d) coordination. This may be expected because of the very small chemical shift range of diamagnetic ^{7}Li (5−6 ppm).[37] As a matter of fact, differences of 0.4 and 0.5 ppm were observed by means of ^{6}Li MAS NMR on enriched Li/Ti/O spinel samples.[38,39] The addition of Mn to pure $Li_4Ti_5O_{12}$ (b−e) causes a series of effects: (i) the progressive increase of the overall width of the spinning sidebands manifold, (ii) the increase of the full-width at half-height (fwhh) of the central line, (iii) the growth of a shoulder at ∼8 ppm (peak B) for Mn contents ≥10% (see Figure 4), and (iv) the rising of a spectral feature due to the $LiMn_2O_4$ phase[40] for Mn ≥ 15% (inset in Figure 3e), in agreement with the XRPD and EPR results.

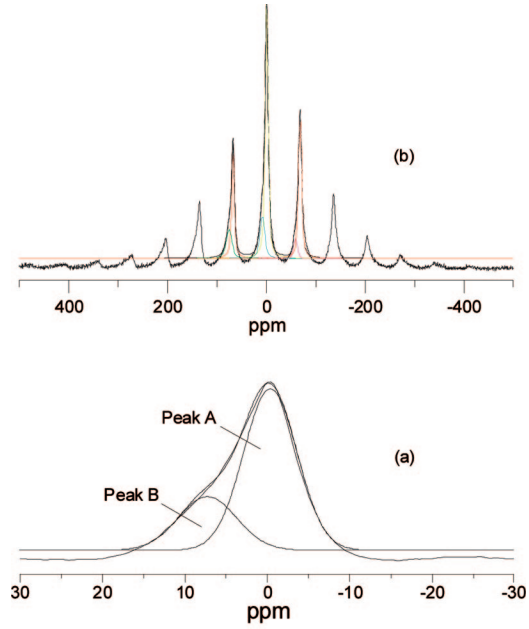

Figure 4. ^{7}Li MAS NMR. Part (a): detail of the central line (peak A) of the sample 10C where the shoulder at ∼8 ppm (peak B) is very evident; Part (b): detail of the Gaussian deconvolutions of the central line and the first couple of spinning sidebands of the same sample.

Figure 4 shows, as an example, a detail of the central line and the first couple of spinning sidebands of the sample 10C, together with their Gaussian deconvolutions (part b) and a detail of the central line (peak A) where the shoulder at ∼8 ppm is very evident (part a). The chemical shifts of both the central line and the peak originating the shoulder (peak B) do not change significantly for all the examined samples.

Figure 5a shows the behavior of the fwhh of peak A vs the Mn content.

It is interesting to note that the addition of a quantity as low as 3% of Mn is enough to determine the increase of the line width of peak A from ∼300 to ∼1200 Hz, and that higher additions of Mn do not cause further enlargements. However, a fwhh spread of ∼10% is observed across the samples with 10% Mn (see Discussion). These values, as well as those reported for higher Mn contents, do scale as the Mn abundances on the 8a site as determined by the Rietveld refinement (see Table 2). Figure 5b shows how the area of the peak B changes with the overall Mn amount. This behavior displays a saturation above 10−15% Mn. It is noteworthy that, also in this case, the areas of the samples prepared with the same nominal Mn amount, but under different experimental conditions, do scale as the Mn abundances on the 8a site obtained by the Rietveld method. Our sensitivity tests showed that the inclusion of more spinning sidebands in the computation causes variations less than 5% of the area of peak B.

The above-reported effects (i) and (ii) are clearly due to the through-space magnetic dipolar interaction between the lithium ions, irrespective of their coordination, and the

(35) Azzoni, C. B.; Catti, M.; Paleari, A.; Pogliani, C. *J. Phys.: Condens. Matter* **1997**, *9*, 3931.
(36) Abragam, A.; Bleaney, B. *Electron Paramagnetic Resonance of Transition Ions*; Clarendon Press: Oxford, 1970; Vol. 469, pp 399, 469 and 430−434.
(37) Harris, R. K.; Mann, B. E. *NMR and the Periodic Table*; Academic Press: London, 1978; 152 pp.
(38) Kartha, J. P.; Tunstall, D. P.; Irvine, J. T. S. *J. Solid State Chem.* **2000**, *152*, 397.
(39) Krtil, P.; Dedecek, J.; Kostlanova, T.; Brus, J. *Electrochem. Solid-State Lett.* **2004**, *7*, A163.
(40) Mustarelli, P.; Massarotti, V.; Bini, M.; Capsoni, D. *Phys. Rev. B* **1997**, *55*, 12018.

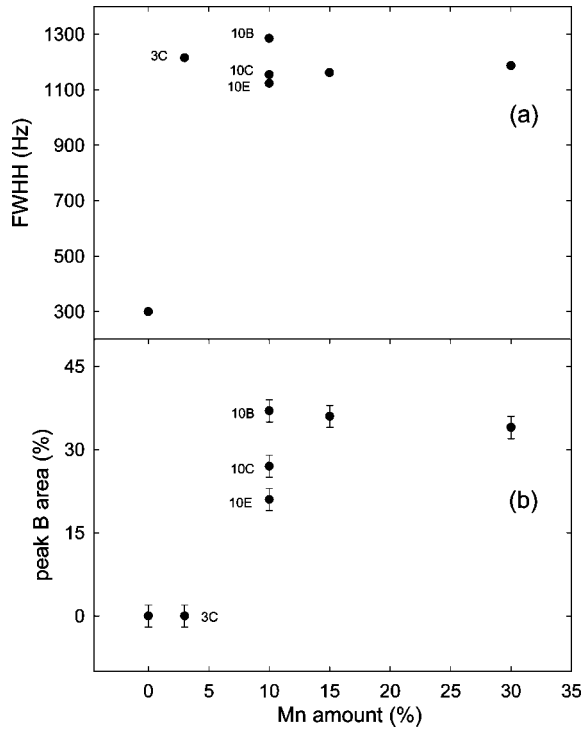

Figure 5. ^{7}Li MAS NMR: behavior of (a) the full-width at half-height of peak A and (b) the area of peak B vs the Mn amount.

unpaired electrons of the Mn ions. This interaction, which is delocalized in nature, is larger than 150 kHz already for the samples with 10% Mn (see Figure 3c) and, as expected, is only partially removed by MAS rotation. The saturation of the central line width reported in Figure 5a is further proof that the interaction is delocalized, although we cannot fully exclude the clustering of the Mn defects.

The effect (iii) is likely due to one of FC and PS hyperfine interactions. The task to address the nature of this hyperfine shift, as well as to relate it to specific local environments, is not trivial since the involved Li atoms may be both tetrahedrally and octahedrally coordinated, and the transferred electron spin densities may come by Mn atoms residing in 8a and/or in the 16d sites. The combined information from NMR, EPR, and XRPD can allow this point to be ascertained.

4.4. IS. Impedance spectroscopy was applied to the pure and some Mn-doped samples to evaluate the Mn influence on the conductivity of the $Li_4Ti_5O_{12}$ compound. All the impedance plots are characterized by a distorted half-circle, due to the presence of both bulk and grain boundary contributions to the total resistivity. The Arrhenius plot of the conductivity data is shown in Figure 6.

Generally, all the Mn-doped samples are less conductive than the pure one at least for temperatures lower than 850 K. The conductivity decreases with increasing the Mn content: among the 10% doped samples, the highest conductivity in the whole temperature range is observed for the 10E sample.

5. Discussion

The Mn substitution up to 30% in $Li_4Ti_5O_{12}$ does not change the *Fd*3*m* spinel structure. We point out that our samples do not show the ordered spinel form ($P4_332$ S.G.)

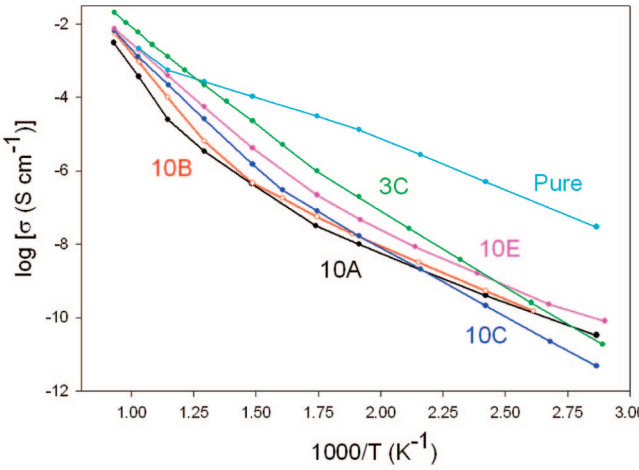

Figure 6. Arrhenius plot of the conductivity data of some selected samples.

reported for $LiMn_{2-y}Ti_yO_4$ ($1 \leq y \leq 1.5$).[25] This different behavior can probably be attributed to both the different synthesis procedure (literature samples are obtained by quenching) and stoichiometry.

The lattice parameter values obtained from Rietveld refinement (Table 1) decrease with increasing the dopant amount, as expected on the ground of crystal radii and on the basis of the Vegard law.

The cation distribution model for the Mn ion on both the cationic sites leads to positive reliable values of isotropic thermal factors (Table 1). The impurity amount of Li_2TiO_3 and $LiMn_2O_4$ increases with increasing the dopant content as reported in Table 2. To estimate the influence of the impurity phases on the real stoichiometry of the doped lithium titanate, the spinel stoichiometry can be recalculated on the basis of the impurity phase percentage reported in Table 2. Even in samples with relevant impurity amount (10C, 15C , and 30C samples), the nominal and recalculated Mn stoichiometry agrees quite well. In fact, the recalculated amount of Mn in the spinel structure is 0.181, 0.278, and 0.496 against 0.167, 0.250, and 0.500 used in the synthesis for 10C, 15C, and 30C samples, respectively. In particular, by refining the XRPD patterns starting from the recalculated stoichiometry, the Mn distribution on the two crystallographic sites agrees with that reported in Table 2, within the standard deviations. The $[Li_{0.963(4)}Mn_{0.037(4)}]_T[Li_{0.313(4)}Mn_{0.144(4)}Ti_{1.543}]_OO_4$ and $[Li_{0.959(5)}Mn_{0.041(5)}]_T[Li_{0.267(5)}Mn_{0.455(5)}Ti_{1.278}]_OO_4$ refined stoichiometries are obtained for 10C and 30C samples.

Useful suggestions about the Mn ions distribution come from the EPR data. The observed signals could be attributed to Mn^{2+} cations distributed on both octahedral and tetrahedral sites. Nevertheless, a strong linear correlation exists between the Mn occupation in tetrahedral sites deduced from Rietveld refinement (see Table 2) and the relative Mn^{2+} amount in the samples accurately achieved by comparing the EPR signal intensities of the samples themselves. This allowed us to state that only the tetrahedral sites are occupied by the Mn^{2+} ions, whose actual occupation value has been estimated from careful comparison with standard signal areas and reported in Figure 7, where the linear correlation is shown.

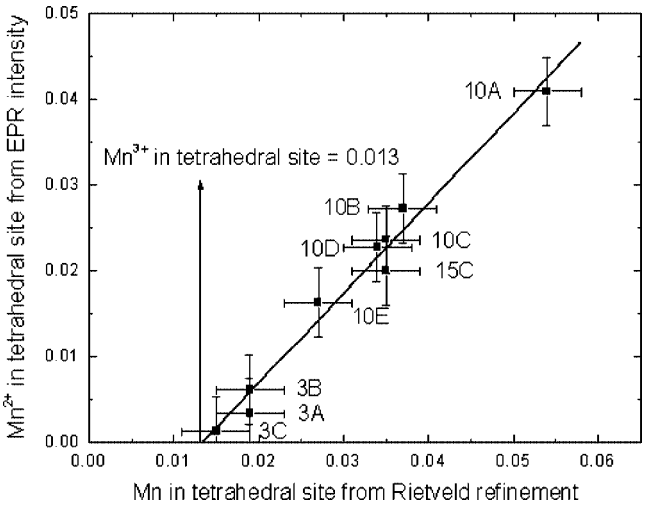

Figure 7. Mn^{2+} amount in tetrahedral site as deduced from EPR signals intensities vs the overall Mn amount in tetrahedral site deduced from Rietveld refinement.

As indicated in this figure, the same Mn^{3+} quantity (0.013) in tetrahedral sites is deduced for all the samples, on the basis of the occupation values of Mn^{2+} in tetrahedral sites and taking into account that no evidence of Mn^{4+} ions comes from both NMR and EPR data. In fact, in ^{7}Li NMR spectra no signals in the range 500−2000 ppm,[32] typical of Mn^{4+} ions in spinels or layered structures, are observed and also the strong ^{7}Li NMR signal at 847 ppm,[41] due to the $Li_4Mn_5O_{12}$ phase, is absent at all in our spectra. For what concerns the EPR measurements, the hyperfine structure observed for the 3% Mn doped, as explained in the results, allows us to ascribe the whole signal observed in these samples to Mn^{2+} ions.

The absence of Mn^{4+} ions in these compounds is in contrast to what is observed from other authors[23] but this may not be surprising if we take into account that different synthesis routes have been used. Anyway, the low thermal stability of Mn^{4+} and its easy partial reduction to Mn^{3+} in a highly oxidizing atmosphere even in the $Li_4Mn_5O_{12}$ spinel prepared by solid state synthesis is discussed in previous works.[27–29]

The occurrence of two different ions in tetrahedral sites (Mn^{3+} and Mn^{2+} ions), with distinct arrangements of the coordinated oxygen ions, can be a source of local distortions which may contribute to the structural disorder together with the local distortion of the Mn octahedral coordination sites. The observed "glass shape" of the Mn^{2+} EPR spectra, related to the component with $g_{eff} \sim 4.3$, can be derived just from the presence of Mn^{3+} ions located in tetrahedral sites. In fact, signals from Mn^{2+} in the tetrahedral site of the spinel structure have been already detected, for example, for the ordered ($P4_332$ S.G.) $LiMn_{2-y}Ti_yO_4$ spinel,[25] but only a single narrow signal component with $g_{eff} \sim 2$ is observed for $y = 1.5$, i.e., when Mn^{2+} is the only paramagnetic entity in the compound, and only a broadening of the line width is evidenced for different stoichiometries ($y < 0.15$) as a consequence of the presence of Mn^{3+} (and Mn^{4+}) ions located, in that case, in the octahedral sites only.

(41) Lee, Y. J.; Wang, F.; Grey, C. P. *J. Am. Chem. Soc.* **1998**, *120*, 12601.

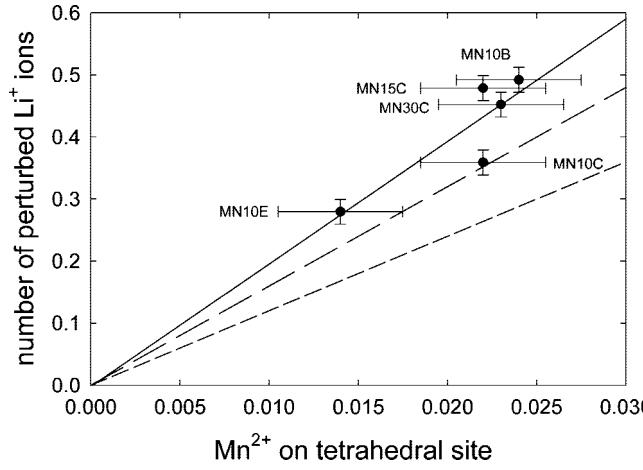

Figure 8. Behavior of the number of Li^+ ions (calculated by the peak B area of Figure 4b multiplied by 1.33) vs the Mn^{2+} amount on the tetrahedral site, as determined by EPR and XRPD. Continuous line: best-fit linear regression. Long dashed line: expected behavior ($m = 16$) in the case of PS interaction. Short dashed line: expected behavior ($m = 12$) in the case of FC interaction.

For what concerns the NMR results, the origin of the hyperfine shift must be attributed to the Mn^{2+} ions occupying the tetrahedral 8a sites. This is clearly shown in Figure 8, where the Li amount expressed by the peak B area of Figure 4b is correlated with the Mn^{2+} paramagnetic ions amount on the tetrahedral site, as determined by EPR and XRPD.

The correlation is linear, and the regression curve passes exactly through the axes origin, which demonstrates that the lithium ions accounting for the peak B are actually disturbed by Mn^{2+} ions on tetrahedral sites. Within the chosen units, the slope m of the linear best fit represents the average number of Li atoms perturbed by each Mn^{2+} ion.

The nature (FC or PS) of the hyperfine shift can be ascertained by considering the local structure and the connectivity around the 8a site. Each tetrahedron is connected via oxygen bonds with 12 octahedral 16d sites at 3.4646 Å, whereas it sees four 8a sites at 3.6187 Å. If the hyperfine shift were only due to FC (through-bonds interaction), for the linear correlation of Figure 8 we should obtain $m = 12$ (short dash line), whereas if the PS term were significant, a value of $m \geq 16$ (long dashed line) should be found. The slope of the best fit is actually ∼19, which means that the hyperfine shift is likely due to the PS term. Whereas PS interactions are well-studied in organometallic solution NMR,[42] they are rarely observed in the solid state. Nayeem and Yesinowski[43] observed a small PS term (∼10 ppm upfield) in the ^{1}H MAS NMR spectrum of $CuSO_4 \cdot 5H_2O$. Pseudocontact shifts in the range 0−100 ppm were reported for stannates containing lanthanide ions.[44]

Further indirect proof that the hyperfine shift is due to a through-space interaction comes from the saturation level (∼35%) of the peak B area reported in Figure 5b. In fact, a value of 24.8% should be obtained if *all* and *only* the Li atoms on the octahedral 16d site (through-bond connected) were involved in the interaction.

(42) Bertini, I.; Luchinat, C. *Coord. Chem. Rev.* **1992**, *150*, 1–292.
(43) Nayeem, A.; Yesinowski, J. P. *J. Chem. Phys.* **1988**, *89*, 4600.
(44) Grey, C. P.; Dobson, C. M.; Cheetham, A. K.; Jakeman, R. J. B. *J. Am. Chem. Soc.* **1989**, *111*, 505.

A question could arise on why the FC term is not observed in the spectra of the samples with more than 10% Mn. An answer to this can lie in the expected low intensity of the signal, which can be masked by the spinning sidebands and/or by the difficult phasing of the spectra. Moreover, we cannot fully rule out a partial clustering of the Mn^{2+} ions which would further lower the signal intensity. In the future, ^{6}Li NMR on enriched samples could help to clarify this point.

Finally, the absence of peaks at shifts multiple of that of peak B (see Figure 4b) suggests us that each perturbed Li ion statistically "sees" only one Mn^{2+} ion in the surroundings. The probability, $P(n, N)$, that each Li atom (in tetrahedral or octahedral coordination) sees n Mn^{2+} as the neighbors is given by the binomial distribution

$$P(n,N) = \binom{N}{n} p^n (1-p)^{N-n}$$

where N is the number of 8a sites connected through the space to the 8a and 16d sites and p is the Mn^{2+} occupancy of the 8a site reported in Table 2, decreased of the 0.013 Mn^{3+} site occupancy (see above Discussion). In addition to the above-reported 8a−8a connectivity, from the spinel structure we also know that each octahedral 16d site has six tetrahedral sites at 3.4646 Å. Simple calculations show that $P(1, 6) \leq 13\%$ and $P(1, 4) \leq 9\%$ for the 16d−8a and 8a−8a connectivity, respectively. Moreover, the ratio $P(1, N)/P(2, N)$ is ∼18 for Li in the 16d site and ∼27 for Li in the 8a site, which means that an eventual NMR peak due to Li atoms perturbed by two Mn^{2+} should account at most for 1−2% of the overall signal, i.e., at the limit of the sensitivity threshold.

The ionic conductivity in $Li_4Ti_5O_{12}$ is due to Li migration from the tetrahedral to the empty octahedral 16c site,[3] so it should be of interest to consider the dependence of the conductivity on the Li tetrahedral content, evaluated from Rietveld refinement (Table 2); the data are shown in Figure 9, for three selected temperatures (473, 673, and 873 K).

For the three isotherms the same trend is observed: the conductivity significantly increases with increasing the tetrahedral Li content and this is consistent with the highest conductivity values observed for the 10E, among the 10% doped samples. Finally, concerning the Mn influence on the conductivity of the $Li_4Ti_5O_{12}$ compound, it is worth noting that the Mn ions insertion in the +2 and +3 oxidation states changes the charge balance in the cationic and possibly in the anionic framework. Conductivity measurements in N_2 flow showing an increase in conductivity suggest the formation of oxygen vacancies in the samples. For example, for the 10C and 30C samples, an oxygen defect of 0.4 and 2.5% respectively is evaluated on the basis of the refined stoichiometry starting from the recalculated values and the known oxidation state of Mn ions.

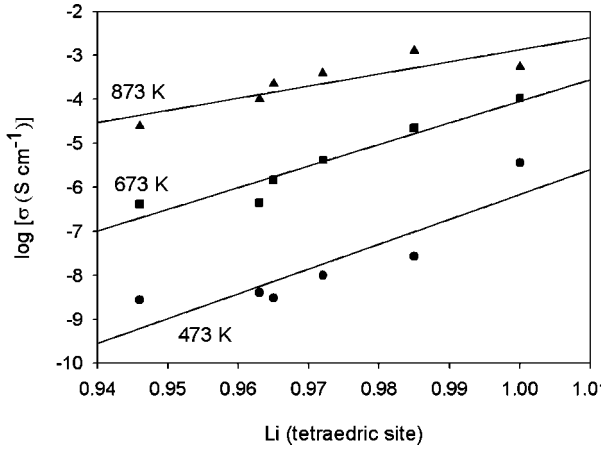

Figure 9. Conductivity behavior as a function of the tetrahedral Li content for the three indicated temperatures.

6. Conclusions

The combined use of XRPD, EPR, and NMR techniques allowed a deep characterization of the Mn-doped $Li_4Ti_5O_{12}$ compound. The Mn ions are present in the +2 and +3 oxidation states. Mn^{3+} ions distribute on both 8a and 16d sites, while Mn^{2+} ions exclusively occupy the tetrahedral one, as deduced by the refined Mn occupancy on the 8a site and the Mn^{2+} EPR signal intensities. On the tetrahedral site an approximately constant amount of Mn^{3+} (0.013) is obtained, while the Mn^{2+} reaches a constant value for 10% substituted samples or higher. The ^{7}Li NMR measurements show a peak at ∼8 ppm for 10, 15, and 30% Mn-substituted samples: this feature is due to a pseudocontact shift. The peak is indeed attributed to the Li^+ ions on both tetrahedral and octahedral sites perturbed by Mn^{2+} paramagnetic ions.

The decrease of the Li content in the tetrahedral site is related to the presence of Mn ions on the same site and it is then responsible for the conductivity decrease observed for the Mn-substituted samples with respect to that of the pure $Li_4Ti_5O_{12}$ compound.

Acknowledgment. A partial funding by the CARIPLO Foundation ("Project "Nuove membrane elettrolitiche nanocomposite a base di liquidi ionici" 2006) is gratefully recognized.

CM703650C